Economic Geology, v. 118, no. 4, pp. 823–836

Stratiform Host-Rock Replacement via Self-Sustaining Reactions in a Clastic-Dominated (CD-type) Zn Deposit

Joseph M. Magnall,[1,†] Richard Wirth,[1] Nicholas Hayward,[2,3] Sarah A. Gleeson,[1,4] and Anja Schreiber[1]

[1]*GFZ German Research Centre for Geosciences, 14473 Potsdam, Germany*

[2]*Teck Australia Pty Ltd, P.O. Box 1677, Western Australia 6872, Australia*

[3]*Centre for Exploration Targeting, University of Western Australia, Crawley, Western Australia 6009, Australia*

[4]*Institute of Geological Sciences, Freie Universität Berlin, Malteserstrasse, 74-100, Berlin 12249, Germany*

Abstract

Stratiform to stratabound replacement of a mixed siliciclastic-carbonate host rock is a defining characteristic of many sediment-hosted base metal deposits. Mineralized rocks in clastic-dominated (CD-type) Zn-Pb ore deposits, which represent our highest value base metal resources, are generally thin (10^1 m), laterally extensive (10^3 m), and stratiform to stratabound in fine-grained siltstone and mudstone facies. At the recently discovered Teena CD-type Zn-Pb deposit (Proterozoic Carpentaria province, Australia), the host rock was undergoing burial diagenesis when altered and mineralized by hydrothermal fluids that moved up to 2 km lateral to the fluid input conduit (growth fault) through intraformational intervals. In much of the deposit, carbonate dissolution was an important reaction permeability control, although significant amounts of mineralization also occur in carbonate-free siliciclastic beds. In this study, transmission electron microscopy (TEM) data has been generated on a drill core sample that preserves a sharp reaction front between mineralized and unmineralized domains of the fine-grained siliciclastic compositional end member (carbonate free). Petrographic and mineralogical data provide evidence that oxidized hydrothermal fluids moved through the protolith via reaction permeability that developed from feldspar dissolution. The nature of reactive fluid flow was determined by reactions that took place at the fluid-mineral interface. Pyrite formation during the earliest stage of the hydrothermal paragenesis increased the mineral reactive surface area in the protolith. Acidity was then generated in situ via self-sustaining reactions involving pyrite oxidation, transient Fe sulfate formation, and sphalerite precipitation, which provided positive feedbacks to enhance porosity creation and further fluid infiltration and mineralization. In the absence of carbonate, however, ore fluid pH was buffered by K-feldspar dissolution (~4.5), thereby ensuring sphalerite precipitation was not inhibited under more acidic conditions. All CD-type deposits in the Carpentaria province are hosted by a protolith comprising carbonate, K-feldspar, pyrite, and organic matter; these phases set the boundary conditions for the development of self-sustaining reactions during ore formation. Importantly, these self-sustaining reactions represent a Goldilocks zone for ore formation that is applicable to other sediment-hosted deposits that formed via replacement of mixed siliciclastic-carbonate host rocks (e.g., stratiform Cu).

Introduction

Many ore deposits are the product of highly dynamic systems that are characterized by steep geochemical gradients, disequilibrium, and reactive fluid flow through rocks. The mineralogical and compositional changes associated with reactive fluid flow are highly dependent on reactions taking place at the fluid-mineral interface (Altree-Williams et al., 2015). In porous media, reactive fluid flow is also controlled by the evolution of mineral reactive surface area rather than total mineral volume (Waldmann et al., 2014; Beckingham et al., 2016). In sediment-hosted mineral systems (e.g., Cu, U, Au, Zn-Pb) the pore-scale evolution of mineral reactive surface area is not well understood. Part of the challenge is that pore space evolution in fine-grained siliciclastic rocks is complex, due to a combination of depositional and diagenetic processes (Loucks et al., 2012); in ore-forming environments, this challenge is compounded by the destruction of primary mineralogical and textural information during fluid-rock interaction. Nevertheless, improvements in microscale to nanoscale imaging and geochemical analysis of rocks mean we are now developing an unprecedented ability to resolve and understand these processes at the required scale (Steefel et al., 2015).

The highest value base metal resources (Zn, Pb, Cu) in sedimentary basins are located in fine-grained units of mixed composition (siliciclastic, dolomitic, carbonaceous). The Proterozoic Carpentaria Zn province is a classic example, where high-grade clastic-dominant (CD-type) Zn deposits are hosted by fine-grained carbonaceous, dolomitic, and commonly pyritic siltstones (Leach et al., 2010). The Carpentaria Zn deposits are characterized by fine-grained sphalerite (ZnS) cement, which may be confined to particular beds or laminae and continuous over hundreds of meters (i.e., stratiform and/or stratabound). For a long time, it was generally accepted that the fine-grained protolith in CD-type systems was relatively impermeable; combined with the conformable nature of the sulfide mineralization, these two factors had a major influence on genetic models for CD-type deposits. For example, to explain the delicate lamination of the sulfide mineralization, some genetic models have proposed sedimentary exhalative (SEDEX) processes, whereby ore-stage sulfides

†Corresponding author: e-mail, magnall@gfz-potsdam.de

 Submitted: March 18, 2022/Accepted: September 7, 2022

precipitated at the sea floor following the venting of hydrothermal fluids (Large et al., 1998; Ireland et al., 2004). Recent genetic models in the southern McArthur basin described the formation of sulfide mineralization primarily via carbonate replacement (Magnall et al., 2021; Spinks et al., 2021). As a result, the carbonate content of the protolith, which is likely to be highest in shallow-water depositional facies, is a key exploration criterion (Hayward et al., 2021). The reactive flow processes whereby mineral replacement can form laterally extensive stratiform mineralization in low-permeability host units remains unclear.

The Teena CD-type deposit, which has an inferred resource of 58.0 million metric tons (Mt) at 11.1% Zn and 1.6% Pb (Rox Resources, 2016), is the most recent discovery in the Carpentaria Zn province (Fig. 1). It is located near the McArthur River (HYC) deposit and in the same stratigraphic unit (lower HYC Pyritic Shale Member of the Barney Creek Formation; Fig. 1). The protolith to the stratiform to stratabound sulfide mineralization of the McArthur River (HYC) and Teena deposits comprises a mixture of interbedded dolomite, silicate, and reduced (organic matter, pyrite) components (Magnall et al., 2021). The sulfide mineralization is located at a stratigraphic redox boundary, where oxidized hematite stable facies transition to more reduced pyrite stable facies (Fig. 2). Recent studies interpreted a broad range of geologic and geochemical data sets and developed an integrated model of diagenesis and hydrothermal processes during subbasin evolution (Hayward et al., 2021; Magnall et al., 2021). Early diagenetic cementation by dolomite and K-feldspar occluded much porosity and resulted in a low intrinsic permeability in the protolith. A chemical mass balance analysis showed that the majority of sulfide mineralization formed via carbonate replacement, although there is petrographic evidence of subordinate feldspar replacement in carbonate-poor interbeds (Magnall et al., 2021). Replacement processes in mineral systems, like many geologic processes, may involve self-organization. Self-organization may develop where two or more ore-forming processes are coupled (Ortoleva et al., 1987), meaning it is necessary to evaluate feedbacks between the two modes of mineralization in the Teena subbasin to understand the development of

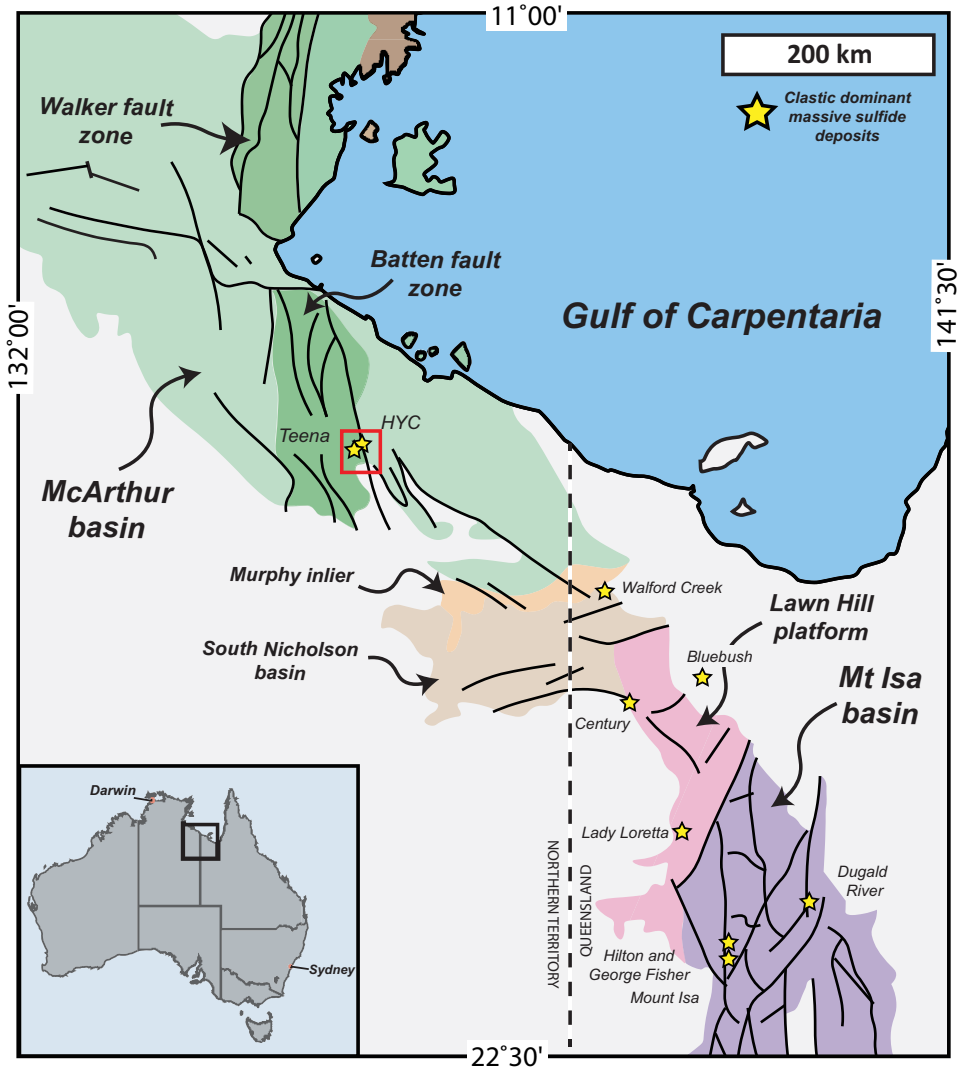

Fig. 1. A regional geologic map of the Carpentaria province (Australia) with locations of major clastic-dominant (CD-type) massive sulfide deposits and prospects (yellow stars). The red box denotes the location of the Teena and McArthur River deposits in the southern portion of the Batten fault zone.

optimal ("Goldilocks") zones of ore formation. For example, was there potential for coupled mineralogical reactions that contributed to the breaching of fluid flow thresholds in the subsurface?

The application of microscale to nanoscale techniques to well-characterized samples offers a promising research direction for developing accurate constraints on how self-organization might develop in sediment-hosted mineral systems. In this study, we focus on a sample from the Teena subbasin that preserves a sharp interface between mineralized and unmineralized host rock (Fig. 2C). This sample provides a unique opportunity to compare microscale to nanoscale mineralogical and paragenetic relationships across a reaction interface. Representative domains were extracted using the focused ion beam (FIB), and ultrathin lamellae were analyzed using transmission electron microscopy (TEM). The microscale to nanoscale observations provide important mineralogical constraints for parameterizing geochemical modeling and understanding how reaction permeability developed over ore-forming distances (10^2–10^3 m) in the Teena subbasin, which may be more broadly applicable to other sediment-hosted mineral deposits.

Background Geology

The Mt. Isa-McArthur superbasin contains mixed carbonate-siliciclastic marine sedimentary rocks that were deposited between 1.82 and 1.58 Ga in an intracontinental setting (Southgate et al., 2000). Several subbasins containing variably mineralized (mostly barren) rocks are located in the southern McArthur basin (Fig. 1). The basement is overlain by more than 10 km of basin fill (Plumb et al., 1980), which is divided into the Tawallah, McArthur, Nathan, and Roper Groups (Pietsch et al., 1991). The Tawallah Group mostly comprises fine- to medium-grained, hematitic, quartz sandstones that are locally evaporitic (sulfate bearing) and subordinate dolomite and volcanic units (see fig. 2 in Cooke et al., 2000). There are some minor carbonaceous units in the Wollogorang and McDermott Formations (Spinks et al., 2016), but overall the Tawallah Group is considered to have provided an oxidized aquifer unit for the ore-forming fluids ($mSO_4^{2-} > mH_2S$; Cooke et al., 2000). The well-sorted, quartz-rich sandstone component of the Tawallah Group likely behaved as an aquifer shortly after deposition, although quartz overgrowths then occluded primary porosity during burial diagenesis (<4-km burial depth; Polito et al., 2006). In contrast, the basal units of the Tawallah Group represent proximal fluvial deposits (conglomerates and continental sandstones) that comprise unstable minerals (e.g., detrital feldspar) that favored the formation of secondary porosity development during burial diagenesis (Polito et al., 2006).

The CD-type deposits (Teena, McArthur River (HYC)) in the Batten fault zone are hosted by the Barney Creek Formation (McArthur Group), which is the first major unit that contains reducing lithologies (carbonaceous and pyritic siltstones). The Barney Creek Formation comprises a range of lithofacies, from shallow-water stromatolitic dolostones to fine-grained carbonaceous silt and mudstones (Kunzmann et al., 2019). The overall age of the Barney Creek Formation is constrained by the youngest detrital U-Pb zircon ages of 1639 ± 6 and 1636 ± 4 Ma for the respective underlying (Teena Dolostone) and overlying (Lynott Formation) lithological units

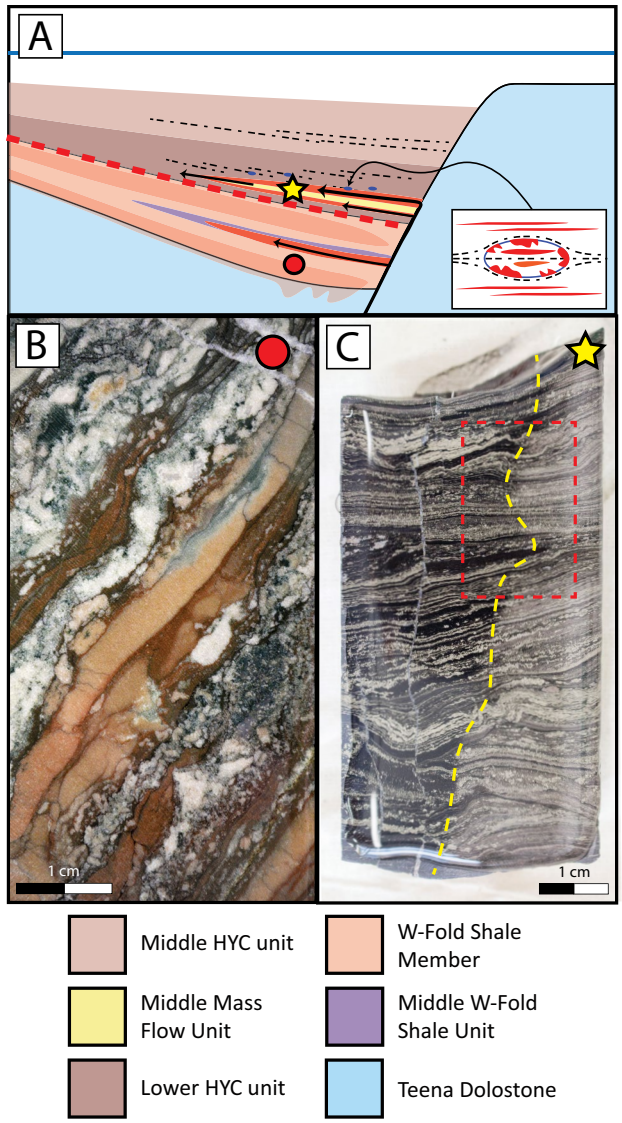

Fig. 2. (A) Cartoon showing the development of sulfide mineralization during burial diagenesis. Red circle and yellow star denote approximate location of samples shown in B and C. Inset depicts the partial replacement of dolomite nodules by sphalerite replacement (modified from Magnall et al., 2021). (B) Drill core sample showing hematite alteration (orange-brown) in the W-Fold Shale Member (TNDD015 at 772 m). (C) Drill core sample with the sharp interface representing a sulfide mineralization reaction front (TNDD025 at 730 m). Box shows location of the thin section from which focused ion beam (FIB) foils were extracted.

(Page et al., 2000). Additionally, tuffaceous beds within the Barney Creek Formation contain zircons with ages of 1638 ± 7, 1639 ± 3, and 1640 ± 3 Ma (Page and Sweet, 1998).

A period of extension during deposition of the Barney Creek Formation resulted in the development of a number of fault-bound depocenters (subbasins) that host CD-type mineralization in the Barney Creek Formation (Hayward et al., 2021). The primary host rock to the Teena and HYC deposits is the Lower HYC Pyritic Shale Member (herein referred to as the Lower HYC unit), which is a compositional mixture of siliciclastic (arkosic), dolomitic, carbonaceous, and pyritic components (Kunzmann et al., 2019; Magnall et al., 2021). The footwall stratigraphy to the Lower HYC unit comprises

the shallow-water Teena Dolostone and overlying W-Fold Shale Member of the Barney Creek Formation, which represents a transitional unit that is a compositional mixture of arkosic siltstone and sandstone and dolostone beds (e.g., Fig. 2B). The upper and lower portions of the W-Fold Shale Member contain dolomite with hematite inclusions and are more oxidized than the overlying Lower HYC unit where pyrite is the dominant Fe-bearing phase.

The Teena and McArthur River (HYC) deposits

The main stage of hydrothermal sulfide mineralization in the Teena subbasin was emplaced in the Lower HYC unit during burial diagenesis and formed principally via carbonate replacement (Hayward et al., 2021; Magnall et al., 2021). Sphalerite mineralization formed after growth of early pyrite and nodular dolomite and initial sediment compaction (Hayward et al., 2021). At the subbasin scale, there is a clear link between structurally controlled fluid influx and enhanced fluid-rock interaction, indicating the potential for positive feedbacks (e.g., Hayward et al., 2021). A similar carbonate-replacement model has also recently been described at the neighboring McArthur River (HYC) deposit (Spinks et al., 2021). At both deposits there is a characteristic two-stage pyrite paragenesis (Williams, 1978; Large et al., 1998; Ireland et al., 2004; Hayward et al., 2021; Spinks et al., 2021), which includes (1) a pre-ore stage of fine-grained microcrystalline (<5 µm) pyrite (py1) that is commonly concentrated along crinkly, organic-rich laminae and (2) coarser-grained aggregates of spheroidal pyrite (py2a) and anhedral overgrowths (py2b) that are both part of the hydrothermal assemblage. There is also a small amount of pyrite (py2c) that is coeval with sphalerite and occurs as microscopic acicular crystals on the margins of py2b (Magnall et al., 2022). At the Teena and McArthur River (HYC) deposits, py2 contains high concentrations of Pb, As, and Tl (Magnall et al., 2020; Spinks et al., 2021). It was recently proposed that the ore-stage paragenesis at McArthur River (HYC) followed a two-stage sequence that involved (1) reduction of the acidic ore-forming fluid (+ py2 formation) followed by (2) carbonate dissolution and neutralization of the ore fluid (Fig. 3, green arrow; Spinks et al., 2021).

The fine-grained nature of the mineralized rocks has prevented the analysis of fluid inclusions in hydrothermal mineral phases from the Teena and McArthur River (HYC) deposits, which means basic temperature and salinity constraints for the mineralizing fluid are lacking. High salinities (25 wt % NaCl equiv) are assumed to have derived from residual evaporated seawater or dissolution of evaporites in the footwall stratigraphy, similar to the ore fluids that formed Mississippi Valley-type (MVT) deposits (Cooke et al., 2000). Evaporite pseudomorphs are common in the carbonate-rich units above and below the host Barney Creek Formation. There is also evidence of brine development in the form of extensive K-metasomatism in the Batten fault zone, but these potassic brines predate the hydrothermal sulfide assemblage and may have formed at low temperature (<50°C; Davidson, 1998; Magnall et al., 2021). In terms of the ore-forming fluid, low temperatures (<100°C) and bacteriogenic sulfate reduction are commonly inferred where sulfide precipitation is considered to have formed at the paleo-sea floor (e.g., Ireland et al., 2004). In contrast, host-rock replacement models often invoke higher temperatures (>150°C) and thermochemical sulfate reduction (TSR). For example, organic compounds (polyaromatic hydrocarbons; PAHs) in the ore zone at the McArthur River (HYC) deposit have been used as evidence for high-temperature (>250°C) fluid-rock interaction during deposit formation (Chen et al., 2003). It was recently argued, however, that the PAHs in a sample from a drill hole distal to the McArthur River (HYC) deposit also contained similar PAHs, indicating these compounds were a product of normal burial diagenetic processes (Vinnichenko et al., 2021). Nevertheless, Rock-Eval pyrolysis and reflectance analysis of organic material from the McArthur River (HYC) ore zone indicate severe alteration, which is consistent with temperatures required for TSR (>150°C; Vinnichenko et al., 2021).

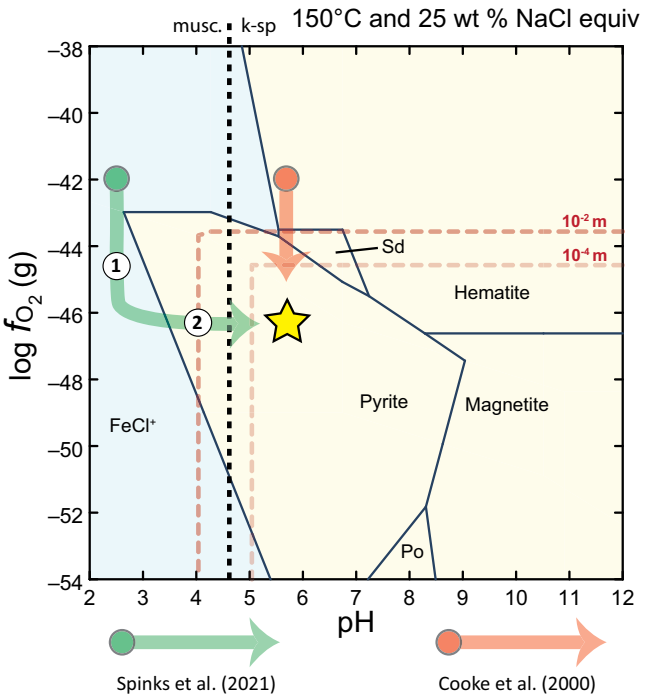

Fig. 3. Mineral stability diagram for major Fe-bearing phases at 150°C. The solubility of Zn in a solution containing 25 wt % NaCl equiv is shown with dashed red lines. Two different scenarios are highlighted (green and red) for the ore-forming fluid, which show starting compositions and trajectories required for Zn sulfide mineralization (yellow star). These scenarios correspond with previous models developed by Cooke et al. (2000) and Spinks et al. (2021). Abbreviations: k-sp = K-feldspar, musc = muscovite, Po = pyrrhotite, Sd = siderite.

Other studies have developed isotopic fractionation models that describe covariation between $\delta^{13}C$ and $\delta^{18}O$ values under different temperature regimes (e.g., Rye and Williams, 1981; Large et al., 2001). This method requires certain assumptions to be made about the speciation of carbonate (H_2CO_3 vs. HCO_3^-) in the hydrothermal fluid, which is dependent on pH (Zheng and Hoefs, 1993). As a result, different models have been developed for the McArthur River (HYC) deposit, which describe the cooling of a weakly acidic HCO_3^--bearing fluid over 120° to 50°C (Large et al., 2001) or cooling of a moderately acidic H_2CO_3-bearing fluid over 240° to 120°C (Rye and Williams, 1981). Higher temperatures (100°–260°C) have also been derived from mineral equilib-

rium pairs from HYC ($\delta^{34}S$ values in sphalerite and galena; Rye and Williams, 1981).

Overall, despite the uncertainty over ore fluid chemistry, base metal solubilities are generally modeled using a temperature estimate of 150°C, which could represent a fluid that has cooled from higher input temperatures, and high salinity (25 wt % NaCl equiv, Cooke et al., 2000). In Figure 3, the stability fields of major Fe phases and Zn solubility contours are shown, which help to illustrate the two ore-fluid pathways suggested for mineralization at the McArthur River (HYC) deposit involving f_{O_2} reduction (red) and f_{O_2} reduction combined with pH increase (green) (modified from Cooke et al., 2000; Spinks et al., 2021). In the f_{O_2} reduction pathway (red; Cooke et al., 2000), the ore fluid is weakly acidic (pH ~ 5.5), and a drop in f_{O_2} provides the primary control on sulfide precipitation. In contrast, the green pathway describes a strongly acidic (pH < 3) ore fluid that must be buffered by carbonate dissolution to ensure effective sulfide precipitation (Spinks et al., 2021).

Methodology

Polished drill core samples were examined using a binocular microscope to identify key mineral phases and paragenetic relationships (e.g., Figs. 2, 4). Thin sections were prepared and then examined using transmitted and reflected microscopy (Fig. 5). Regions of interest were identified either side of the interface between the mineralized and unmineralized domains of the sample (Fig. 6).

FIB and TEM

All analytical work was performed at GFZ Potsdam in the Potsdam Imaging and Spectral Analysis (PISA) Facility. Ultrathin TEM lamellae were extracted from three regions of interest on either side of the mineralized interface of the sample using FIB milling (e.g., Fig. 6). The TEM lamellae are typically ~15 × 5 × 0.10 µm and were cut out with a Helios G4 UC DualBeam (Thermo Fisher-FEI) system (Wirth, 2009). A Pt layer was deposited to protect the areas of interest (dimensions of 20 × 2 × 2 µm). The rough cut occurred under an acceleration voltage of 30 kV and a beam current of 9.3 to 45 nA. The TEM lamellae were removed using an EasyLift system and were fixed to a 3-mm copper grid. The TEM lamellae were then further thinned to nearly 120 nm using 30 kV and beam currents from 0.79 nA to 80 pA. A final polishing under 5 kV and 41 pA thinned and cleaned the FIB lamellae to approximately 100 nm.

The TEM lamellae were investigated with a TECNAI G2 F20 X-twin TEM. The TEM was operated at 200 kV with a field emission gun as electron source. It is equipped with a Gatan Imaging Filter (GIF), a Fishione high-angle annular dark-field (HAADF) system, and an EDAX X-ray analyzer with ultrathin window. The HAADF images were acquired as

Fig. 4. A selection of drill core samples from the Lower HYC unit in TNDD019 (sample depths indicated on core). (A) Disseminated sphalerite in volcaniclastic sandstone (light gray) interbedded with carbonaceous siltstone. (B) Fine-grained carbonaceous siltstone that is cemented by sphalerite. (C) Fine-grained carbonaceous siltstone containing an ovoid dolomite nodule that has been partially replaced by sphalerite around the rim.

Z-contrast images or as Z-contrast + diffraction contrast images, depending on the camera length used. Bright-field, dark-field, and high-resolution lattice fringe images were acquired as energy filtered images applying a 20-eV window to the zero-loss peak. Beside conventional electron diffraction patterns, we used diffraction patterns calculated from high-resolution lattice fringe images by applying a fast Fourier transform (FFT) algorithm. The energy dispersive spectrometry (EDS) analyses were carried out in the scanning transmission mode (STEM). The electron beam was scanned within a selected area, thus minimizing sputtering effects and mass loss during data acquisition. Acquisition time was 60 s.

Geochemical modeling

The Geochemist's Workbench (Bethke, 2007) was used to calculate mineral stability fields and fluid compositions for relevant geochemical conditions. Base species were obtained from the thermo.tdat database, which supports the calculation of activity coefficients according to the extended form of the Debye-Hückel equation. Mineral stability diagrams that show the stability fields of mineral phases and predominance of aqueous species in specified chemical systems were calculated in Act 2. The aqueous species in fluids with different Cl^- concentrations at equilibrium with specific mineral assemblages were calculated using SpecE8. The concentrations of different aqueous species (e.g., K^+) were buffered by an assemblage of major silicate mineral phases (e.g., quartz, K-feldspar, muscovite), and the system was charge balanced for H^+ to provide the pH of the system at equilibrium.

Results

Mineralogy and paragenesis

In Figure 5, characteristic examples of the sphalerite mineralization styles are compared between the sample selected for TEM analysis (Fig. 6A) and additional drill core samples from the Teena deposit (Fig. 4). The selected drill core samples are representative of the different sedimentary facies of the Lower HYC unit, which includes coarse-grained volcaniclastic sandstone (Fig. 4A), fine-grained dolomitic siltstone (Fig. 4B), and nodular dolomite (Fig. 4C). The samples all preserve similar styles of sphalerite mineralization, including sphalerite that is concentrated in the intracrystalline space of coarse-grained aggregates of py2b (e.g., Fig. 5A, D) and a patchy fine-grained sphalerite cement in pyrite-poor domains of the siliciclastic matrix (e.g., Fig. 5C-E). The interface between the fine-grained sphalerite cement and unmineralized siliciclastic matrix is not a unique feature of the TEM sample (Fig. 6A) and is also preserved in other drill core samples (e.g., Fig. 5C, F).

The siliciclastic matrix of the sample is K-feldspar, quartz, and chlorite (Fig. 7C). There are two types of K-feldspar, which are distinguished only by the bright-field TEM images (Fig. 7E, G). One K-feldspar type forms as clasts of crystals that are subangular and preserve exsolution lamellae (serrated texture; Fig. 7E, F). The other type forms highly irregular interlocking crystals that preserve a wormy, mottled texture in the bright-field TEM images (Fig. 7G). The former is interpreted to be detrital, and the latter comprises authigenic overgrowths and cement (Magnall et al., 2021). There are also two types of quartz, with subrounded crystals (e.g., Fig. 7C) and larger interlocking crystals (Fig. 7D, I). Chlorite is the dominant sheet silicate in the Teena sample and forms platy aggregates that wrap around the margins of primary clasts (Fig. 7E, F) or grow into pore space with py2c (e.g., Fig. 8A).

The spherical pyrite crystals (py2a) form aggregates that are concentrated along stratiform horizons (Fig. 6A, B). The py2a crystals are generally <50 µm diameter and preserve multiple growth domains (Fig. 6B, C). The individual growth domains typically constitute a nanocrystalline porous core, which is surrounded by elongate crystals that grow out from the core (Fig. 6C). In the mineralized portion of the sample, Fe sulfate ($FeSO_4$) and Pb oxide have been identified in the intragrain pore space of py2a (Fig. 8B). The Fe sulfate is restricted to microscopic intracrystalline domains of py2 rather than being pervasive throughout the sample. The py2b crystals form larger, more homogeneous, idiomorphic to subidiomorphic aggregates, which can sometimes appear transitional with py2a (Fig. 6E, G).

Both py2a and py2b are overgrown by small, euhedral crystals of py2c (Fig. 6G). This generation of pyrite is restricted to the mineralized portion of the sample and occupies the same pore space as sphalerite. The sphalerite forms a patchy, anhedral cement in the matrix of the mineralized side of the sample (Fig. 6D, F). There is a small amount of K-feldspar and quartz that has formed in textural equilibrium with the sphalerite (Fig. 7D, I, J).

Geochemical modeling

An oxidizing fluid in equilibrium with quartz, K-feldspar, albite, and muscovite at 150°C has a pH that decreases with increasing chloride concentration (Fig. 9). For the approximated salinity constraints for CD-type systems in the Carpentaria (i.e., 10–25 wt % NaCl equiv; Cooke et al., 2000), a fluid in equilibrium with this assemblage would have a pH between 5.5 and 6. The maximum concentration (ppm) of base metals that can be dissolved in the fluid is 455 (Fe), 4 (Pb), and 10 (Zn) at 1.94 *m* chloride (~10 wt % NaCl equiv), and 5,146 (Fe), 145 (Pb), and 1,475 (Zn) at 5.8 *m* chloride (~25 wt % NaCl equiv; Fig. 9).

Discussion

The drill core samples selected for TEM analysis preserve the fine-grained sphalerite cement that resembles mineralization in other drill core samples with carbonate-poor interbeds from the Lower HYC unit (Fig. 4). The crosscutting nature of the reaction front, which is represented by the sharp contact from sphalerite cemented to unmineralized host rock, indicates a transient permeability increase that allowed the hydrothermal fluid to pass through the sample. The lack of significant volume addition or loss (uniform thickness of laminations either side of the replacement front; Figs. 2C, 6A), is consistent with the preservation of external shape and dimensions during pseudomorphic replacement (Putnis, 2009). At temperatures below 300°C (the upper temperature limit for CD-type deposits, e.g., Wilkinson, 2013), mineral replacement occurs via coupled dissolution-reprecipitation reactions (CDR), which can result in positive feedbacks that are integral for ore formation (e.g., Xing et al., 2021). In the following discussion, we evaluate the reactions involved in hydrothermal fluid flow

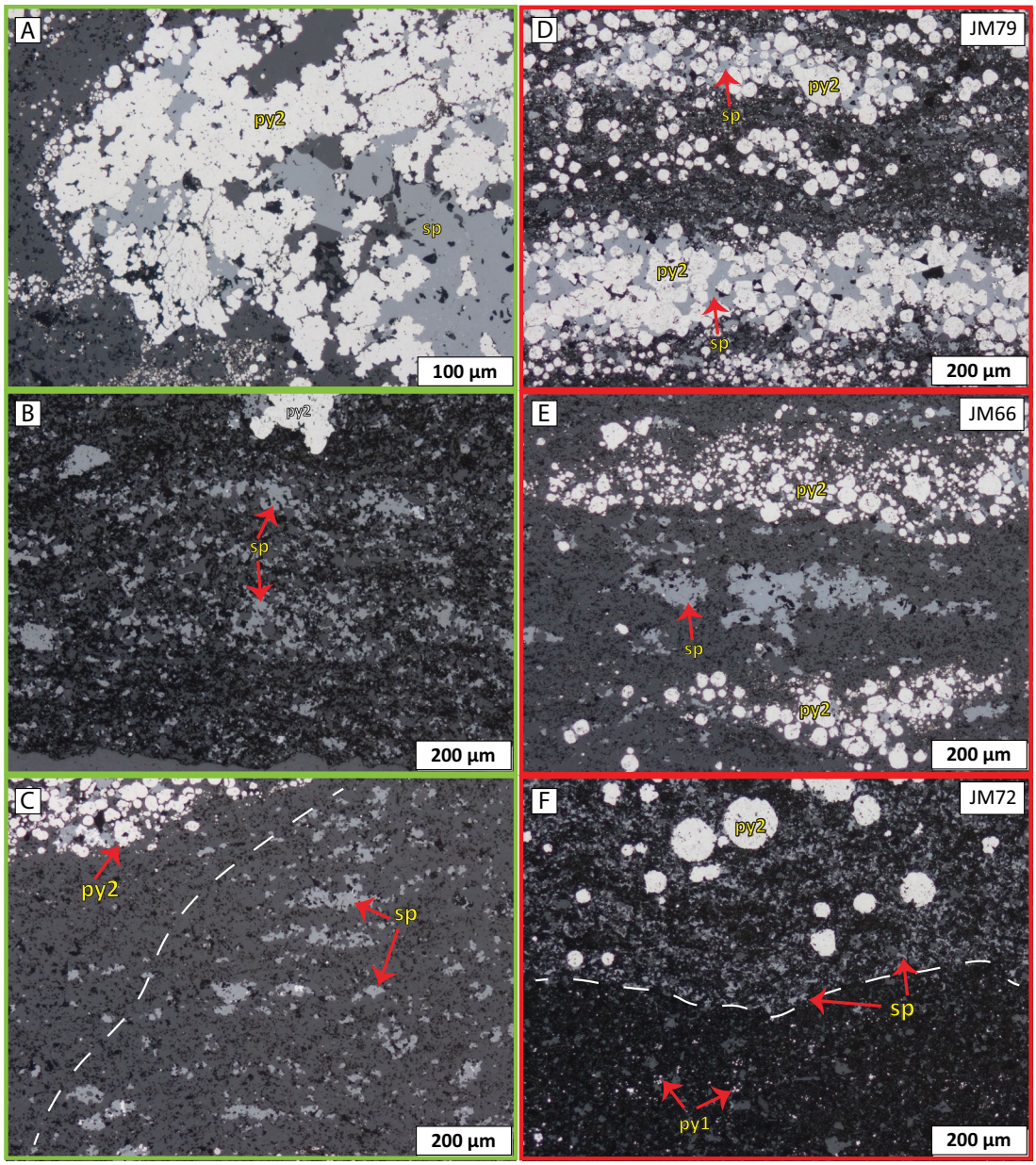

Fig. 5. Reflected-light microscopy showing a comparison between sphalerite mineralization in the drill core sample from Figure 2C (green box) and the samples shown in Figure 4 (red box). Upper labels on D, E, and F refer to sample number. (A) Coarse-grained aggregates of hydrothermal pyrite (py2) that are cemented by sphalerite (sp). (B) Fine-grained siliciclastic bed partially cemented by sphalerite. (C) A transition between sphalerite cement and relatively unmineralized host rock (denoted by dashed white line). (D) Coarse-grained stratiform aggregates of py2 that are cemented by sphalerite. (E) Vuggy sphalerite cement in a siltstone lamination between two horizons of stratiform py2. (F) A stratiform horizon between sphalerite-cemented siltstone lamination that contains coarse-grained spherical pyrite grains and weakly pyritic unmineralized siltstone lamination (denoted by dashed white line).

through the host rock and use mineralogical constraints to determine the local evolution of pH and f_{O_2} during fluid-rock interaction. The broader implications for other deposits hosted in mixed siliciclastic-carbonate units are also discussed.

Pyrite and ore fluid f_{O_2}

In the Lower HYC unit, the pre-ore, microcrystalline aggregates of fine-grained (<5 µm) diagenetic pyrite formed before hydrothermal mineralization and will not be discussed any further. The second generation of pyrite (py2) is spatially associated with the sulfide mineralization and preserves a colloform morphology (py2a) that is then recrystallized and overgrown by more idiomorphic infill (py2b; e.g., Fig. 6D). Although py2a and py2b are crosscut by sphalerite mineralization in the Teena sample (Fig. 4), the strong spatial relationship in the Lower HYC unit indicates the two phases formed as part of the same hydrothermal event (Hayward et al., 2021; Magnall et al., 2022). The overlap between py2 and sphalerite formation is most clearly recorded by the low-volume py2c overgrowths that have formed in the same secondary porosity

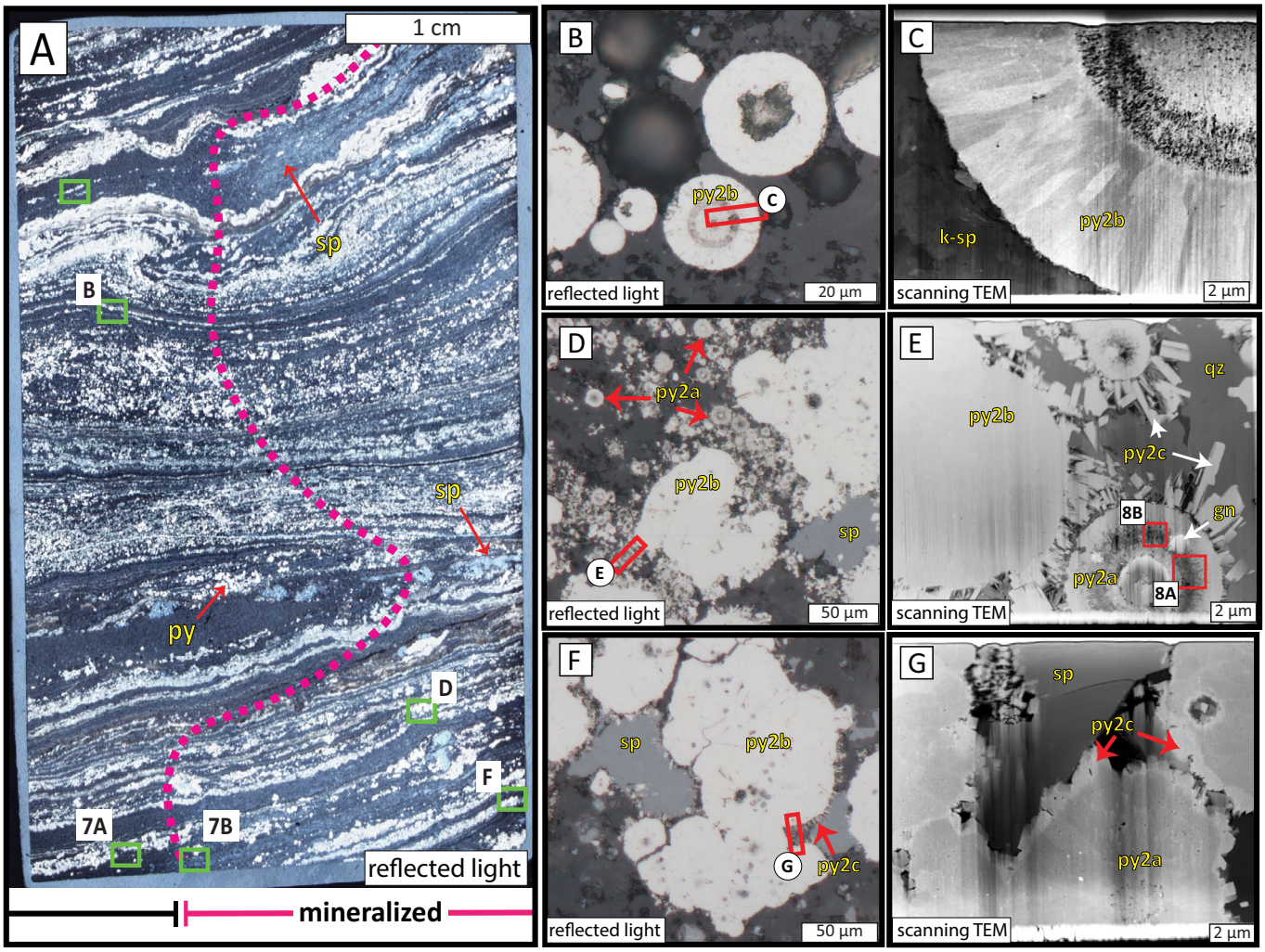

Fig. 6. (A) Thin section of the area shown in Figure 2C, showing the areas that were selected for focused ion beam (FIB) and transmission electron microscopy (TEM). (B) Photomicrograph of spherical pyrite (py2a) in the unmineralized portion of the sample. (C) A backscattered electron (BSE) image of the FIB foil extracted from (B) showing the internal microstructure of the py2a crystal. The different polycrystalline growth domains are characteristic of colloform growth. (D) A photomicrograph of fine-grained py2a crystals and a larger subidiomorphic aggregate of py2b crystals. (E) A BSE image of the FIB foil extracted from (D), showing the internal microstructure of py2a and py2b, which are both overgrown by idiomorphic crystals of py2c that fill the pore space with quartz (qz). (F) A photomicrograph showing the sphalerite (sp) cement in secondary pore space adjacent to aggregates of py2a that are partially overgrown or recrystallized. Small crystals of py2c grow out from the rims of the py2 aggregates. (G) A BSE image of the FIB foil extracted from (F), which shows the sp interface between the py2a aggregates, which preserve some of the internal colloform growth structure, and the py2c overgrowths.

that is filled by sphalerite. The same two-stage pyrite paragenesis and association with sphalerite has also been described at the nearby McArthur River (HYC) deposit (Williams, 1978; Ireland et al., 2004; Spinks et al., 2021).

The variability in the size and morphology of individual colloform py2a crystals was likely controlled by the degree of pyrite supersaturation (Murowchick and Barnes, 1987; Alonso-Azcárate et al., 2001). The smaller grain sizes represent abundant nucleation and a high degree of supersaturation, whereas larger crystals form when a low degree of supersaturation favors crystal growth. The degree of pyrite supersaturation would have been particularly sensitive to small changes in Eh and pH at the SO_4^{2-}/H_2S redox boundary (Butler and Rickard, 2000). The colloform style of py2a is followed by subidiomorphic py2b, which records higher $\delta^{34}S$ values that are consistent with a limited supply of reduced sulfur (Magnall et al., 2020). Under more sulfur-limited conditions, low degrees of pyrite supersaturation and crystal growth are dominant, rather than abundant nucleation of small crystals (Barrie et al., 2009). Altogether, this is consistent with local changes in the supply of Fe and reduced sulfur controlling the saturation state of the fluid and morphological changes in the individual pyrite crystals.

The oxidation of preexisting components (e.g., diagenetic pyrite) is a first-order prediction of host-rock replacement models in the Carpentaria province, as the ore fluid is generally accepted to have been oxidized (Cooke et al., 2000). The restricted occurrence of divalent Fe sulfate ($FeSO_4$) in the mineralized portion of the sample (Fig. 8B) means it is highly unlikely to have formed during sample preparation

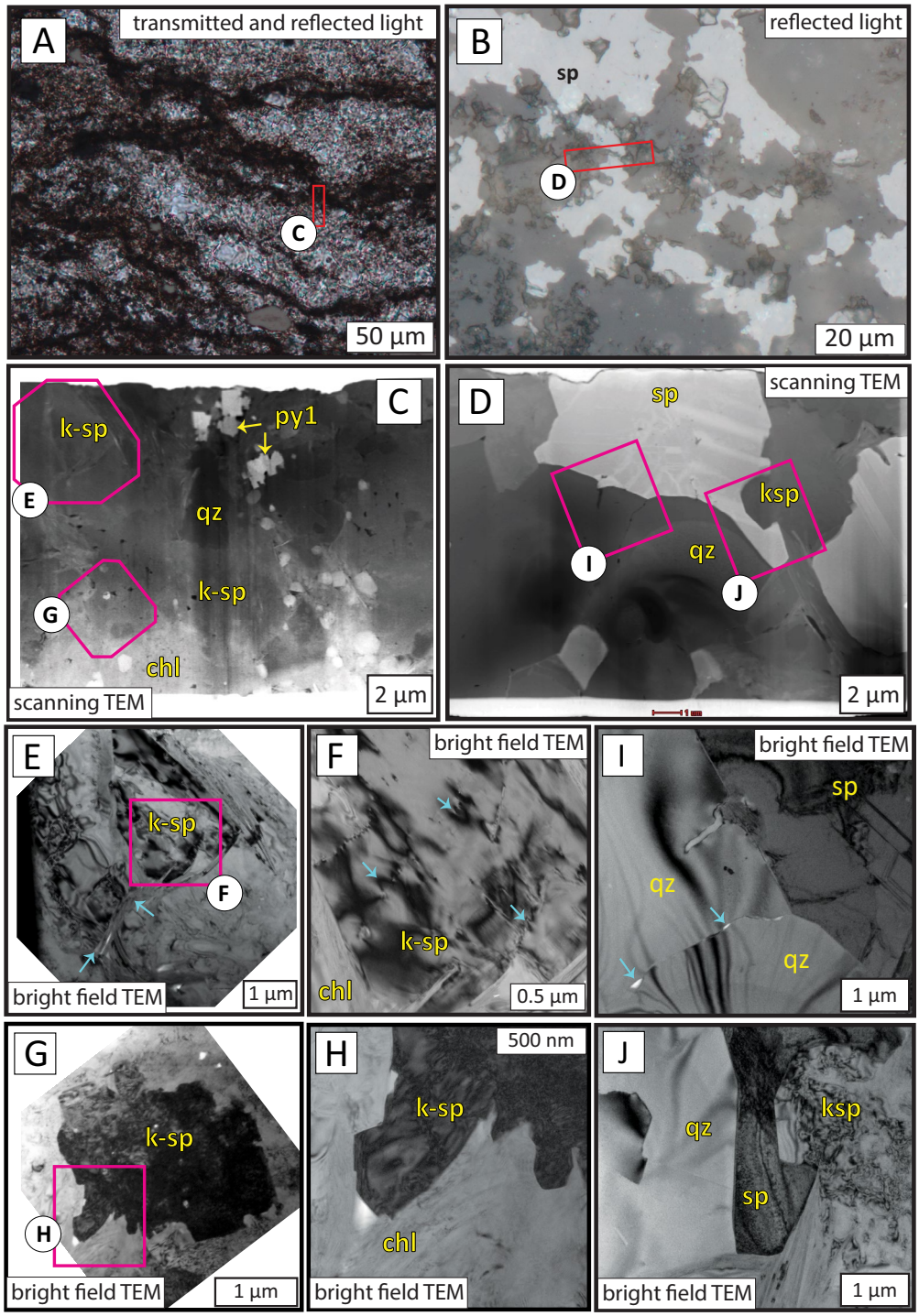

Fig. 7. (A) Photomicrograph showing the two areas where focused ion beam (FIB) foils were extracted in the unmineralized host rock. The location of this photomicrograph in the sample is also shown in Figure 6A. (B) Photomicrograph showing the fine-grained sphalerite cement and the location of the FIB foil across the relict clay-rich lamination. The location of this photomicrograph is also shown in Figure 6A. (C) A backscattered electron (BSE) image of the FIB foil from the unmineralized host rock, which contains a mixture of K-feldspar (k-sp), quartz (qz), chlorite (chl), and fine-grained pyrite (py1). (D) A BSE image of the FIB foil from the fine-grained sphalerite cement, showing a large sphalerite (sp) crystal intergrown with quartz and K-feldspar. (E) A bright-field transmission electron microscopy (TEM) image showing the diffraction contrast of a subangular K-feldspar grain that is partially wrapped by a chlorite grain (yellow arrows). (F) The inset from (E) showing the serrated texture (yellow arrows) that are characteristic of perthite exsolution. (G) A bright-field TEM image showing the diffraction contrast of a highly irregular authigenic K-feldspar crystal with slight subgrain misalignment. (H) The inset from (G) showing chlorite growth and nanoscale porosity on the rim of the K-feldspar crystal. (I) A bright-field (TEM) image of the contact between quartz and sphalerite and dislocations along the boundary between quartz crystals (yellow arrows). (J) A bright-field TEM image of quartz, sphalerite, and a small euhedral K-feldspar crystal.

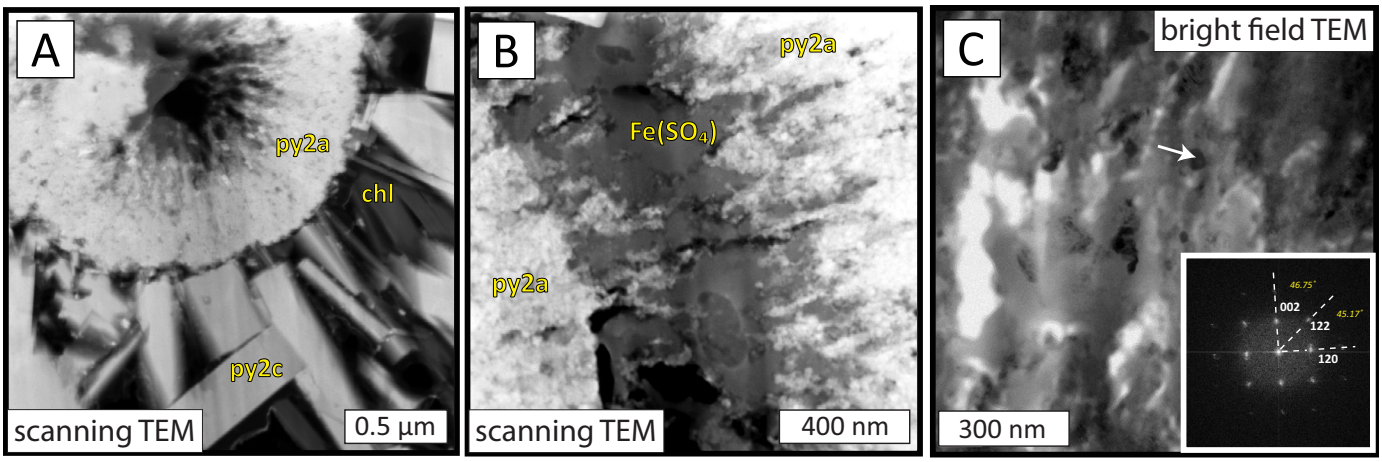

Fig. 8. (A) Microcrystals of spherical pyrite (py2a) rimmed by euhedral pyrite (py2c) intergrown with chlorite. (B) A scanning transmission electron microscopy (TEM) image of the inset shown in Figure 6D, which shows part of the colloform growth of py2a that has been altered to $Fe(SO_4)$. (C) A bright-field TEM image showing another area of $Fe(SO_4)$ alteration (inset from Fig. 6D) and the location (white arrow) of the area selected for electron diffraction (SAED), with results shown in the inset figure. Abbreviation: chl = chlorite.

and is more likely to have formed during alteration from the oxidized hydrothermal fluid. Iron sulfate minerals are most commonly found in low-pH environments, which are associated with epithermal deposits (e.g., Chouinard et al., 2005) or during acid mine drainage (AMD) when sulfide minerals are exposed to oxidizing meteoric fluids (e.g., Joeckel et al., 2005). Studies on AMD environments have shown there is a predictable paragenesis associated with the oxidation of Fe sulfides, which involves the formation of metastable Fe sulfates that are eventually transformed to Fe oxyhydroxides (Jerz and Rimstidt, 2003). Divalent Fe sulfate minerals (e.g., melanterite, $Fe^{2+}SO_4 \cdot 7H_2O$; szomolnokite, $Fe^{2+}SO_4 \cdot H_2O$) are the first to form during pyrite oxidation, before progressive oxidation and dehydration results in the formation of ferrous Fe sulfates and eventually Fe oxyhydroxides (Jerz and Rimstidt, 2003):

$$2FeS_2 + 7O_2 + 16H_2O = 2FeSO_4 \cdot 7H_2O + 4H^+ + 2SO_4^{2-}. \quad (1)$$

Importantly, Fe sulfate minerals are highly soluble and commonly dissolve in aqueous environments (Frau, 2000). In the Teena sample, the Fe sulfate is restricted to the residual intracrystalline pore space of py2a (e.g., Fig. 8), which would have provided a microenvironment where it was likely protected from dissolution during subsequent fluid-rock interaction. The py2 grains preserve varying degrees of recrystallization (e.g., Fig. 8E), which could represent variability in the extent to which Fe sulfate has been replaced by pyrite during progressive reduction of the hydrothermal fluid.

Feldspar dissolution and sphalerite mineralization (ore fluid pH)

It has been suggested that acidity (pH ≈ 2) was an intrinsic feature of the hydrothermal fluids responsible for CD-type mineralization in the McArthur basin (e.g., Fig. 3, green arrow; Liu et al., 2021; Spinks et al., 2021). Most acidic ore-forming fluids are associated with the disproportionation of magmatic volatiles and result in acid sulfate mineral assemblages (e.g., Seewald et al., 2019); however, there is no evidence of coeval magmatism or of the development of widespread acid sulfate assemblages in the McArthur basin. The main aquifers to the ore-forming fluids are generally accepted to have been coarse-grained sandstone and conglomerate units in the Tawallah and lower McArthur Groups (Polito et al., 2006). Compositionally, these units are a mixture of quartz, feldspar, and phyllosilicate phases (Idnurm, 2000). Fluid-rock equilibration involving major silicate minerals (quartz, feldspar, muscovite) typically results in a relatively narrow range of weakly acidic to neutral pH values (Hanor, 2001; Yardley, 2005). For example, the pH of a fluid in equilibrium with the dominant mineral phases in the Tawallah and lower McArthur Groups would have been between 5.5 and 6 (Fig. 9), meaning it is unclear how strong acidity could have been an intrinsic property of CD-type ore fluids in the McArthur basin.

The nonsulfide mineralogy in the sample primarily comprises K-feldspar, quartz, and minor amounts of chlorite, which is representative of the siliciclastic end member of the Lower HYC unit (cf. Magnall et al., 2021). Previous studies have shown that K-feldspar is a major component of the Barney Creek Formation due to a combination of immature volcaniclastic sedimentation and low-temperature K metasomatism (Davidson, 1998; Magnall et al., 2021). In the Teena sample, these two sources of feldspar are represented by subangular detrital feldspar clasts, which preserve fine-scale twinning and flame-like structures that are typical of perthite (Fig. 7F; Lee and Parsons, 2003), and authigenic feldspar that forms highlights irregular grains with complex, dark diffraction contrasts typical of slight subgrain misalignments (e.g., Fig. 7G). Importantly, the sphalerite mineralization in the Teena sample appears to have formed in secondary porosity associated with feldspar dissolution, which is most readily apparent when comparing zones from the same lamination that are either side of the reaction interface (e.g., see Fig. 6 and corresponding areas shown in Fig. 7A, B). Acidic conditions are generally required for feldspar dissolution (pH < 5; Fig. 3), which is a common diagenetic reaction in arkosic sandstone reservoirs (Yuan et al., 2019). There is no kaolinite or illite associated

with feldspar dissolution in the Teena sample, which indicates that Al was mobile under open-system conditions (e.g., Yuan et al., 2015). Rather, quartz and microscopic orthorhombic pyrite crystals (py2c) have both grown into pore space that is associated with sphalerite precipitation (reactions 2 and 3):

$$Zn^{2+} + H_2S = ZnS + 2H^+ \quad (2)$$

$$Zn^{2+} + CH_4 + SO_4^{2-} = ZnS + CO_3^{2-} + 2H^+ + H_2O. \quad (3)$$

The two pathways of sphalerite precipitation represent fluid mixing with pore-bound reduced sulfur or sour gas (reaction 2) and TSR (reaction 3). Reaction (2) is the main driver of acid production and host-rock dissolution in carbonate-dominant systems (Corbella et al., 2004), whereas reaction (3) is more typical of reducing siliciclastic units where organic carbon is present. In mixed siliciclastic-carbonate units like the Lower HYC unit, a combination of reactions (2) and (3) was likely important. The acidity generated in reactions (2) and (3) resulted primarily in the dissolution of dolomite in the Lower HYC unit (Magnall et al., 2021):

$$CaMg(CO_3)_2 + 2H^+ = Ca^{2+} + Mg^{2+} + 2CO_3^{2-} + H_2O. \quad (4)$$

In the absence of carbonate to buffer acidity, however, the pH dropped below the threshold required for feldspar dissolution (pH < 4.5):

$$KAlSi_3O_8 + 4H^+ = 2H_2O + 3SiO_2 + Al^{3+} + K^+. \quad (5)$$

Importantly, in the Teena sample, feldspar has reprecipitated into the same secondary pore space as sphalerite (Fig. 7J), meaning it is unlikely that pH remained at a level that inhibited sphalerite mineralization (<2; Liu et al., 2021).

Implications

The stratiform mineralization in the Lower HYC unit of the Teena subbasin has a high aspect ratio (>100:1). During ore formation, the development and maintenance of transient horizontal reaction permeability along the flow path would have been critical. The Lower HYC unit represents a potential Goldilocks zone, which developed when fluid input initiated a series of self-sustaining reactions involving acid production and acid consumption that balanced mineral dissolution and mineral precipitation (Fig. 10). The formation of py2 during the earliest stage of the hydrothermal paragenesis was particularly important for increasing the mineral reactive surface area in the Lower HYC unit. The generation of acidity during pyrite oxidation (reaction 1) and sulfide precipitation (reactions 2, 3) resulted in both dolomite and feldspar dissolution and the development of secondary porosity. The modal composition of the Lower HYC unit provided a sweet spot for the development of reaction permeability and sphalerite mineralization in a largely rock buffered system; too much dolomite and acid neutralization may have suppressed porosity generation, whereas too little carbonate and excessive acidification may have increased Zn solubility (e.g., Liu et al., 2021). The cations produced during host-rock dissolution must have been flushed away to limit negative feedbacks associated with porosity occlusion, perhaps resulting in distal dolomite, illite, and quartz formation. For exploration models, this Goldilocks zone is associated with transitional lithofacies deposited during a marine transgression. In the southern McArthur basin,

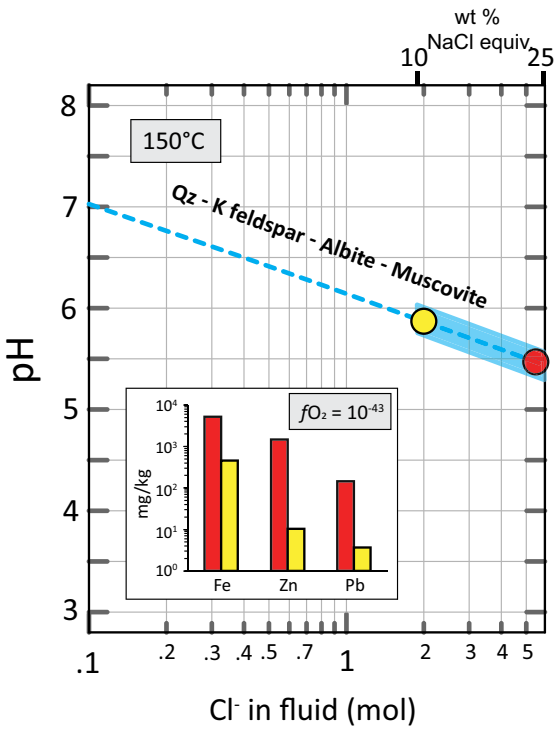

Fig. 9. The pH of a 150°C fluid at varying chloride concentrations in equilibration with quartz, K-feldspar, albite, and muscovite. The inset shows the maximum concentration of base metals that are soluble in the fluid at moderate (yellow) and high (red) salinities (10 versus 25 wt % NaCl equiv, respectively). Abbreviation: Qz = quartz.

these lithofacies are located stratigraphically below the most organic-rich intervals that are associated with the maximum flooding surface (Hayward et al., 2021; Kunzmann et al., 2022). Importantly, the most organic-rich intervals are carbonate poor and would likely have provided an effective seal that further promoted lateral subsurface fluid flow (Hayward et al., 2021; Magnall et al., 2021; Kunzmann et al., 2022).

A number of sediment-hosted base metal deposits (e.g., CD-type Zn, sediment-hosted Cu) formed via stratiform to stratabound replacement of a mixed siliciclastic-carbonate host rock. The most direct comparison is the McArthur River (HYC) CD-type deposit, which is also hosted by the Lower HYC unit in a neighboring subbasin to the Teena deposit (Spinks et al., 2021). The HYC deposit, which preserves a similar sulfide paragenesis and host-rock composition, has all the prerequisites for the development of self-sustaining reactions similar to those described for the Teena deposit. Similarly, the CD-type deposits in the Mt. Isa region are hosted by the Urquhart Shale Formation, which is a dolomitic arkosic siltstone with similar mineralogical composition to the Barney Creek Formation (Rieger et al., 2021). Overall, this means that among arkosic interbeds that lacked carbonate, ore fluid pH in all Carpentaria province Zn deposits may have been locally buffered by K-feldspar to >4.5 (Fig. 3), ensuring effective sphalerite precipitation by replacement of adjacent carbonate nodules and interbeds. More broadly, stratiform Cu deposits are also widely accepted to have formed via replacement of a mixed siliciclastic-carbonate host rock (Oszczepalski, 1999; Selley et al., 2005; Borg et al., 2012). The Neoproterozoic Ore

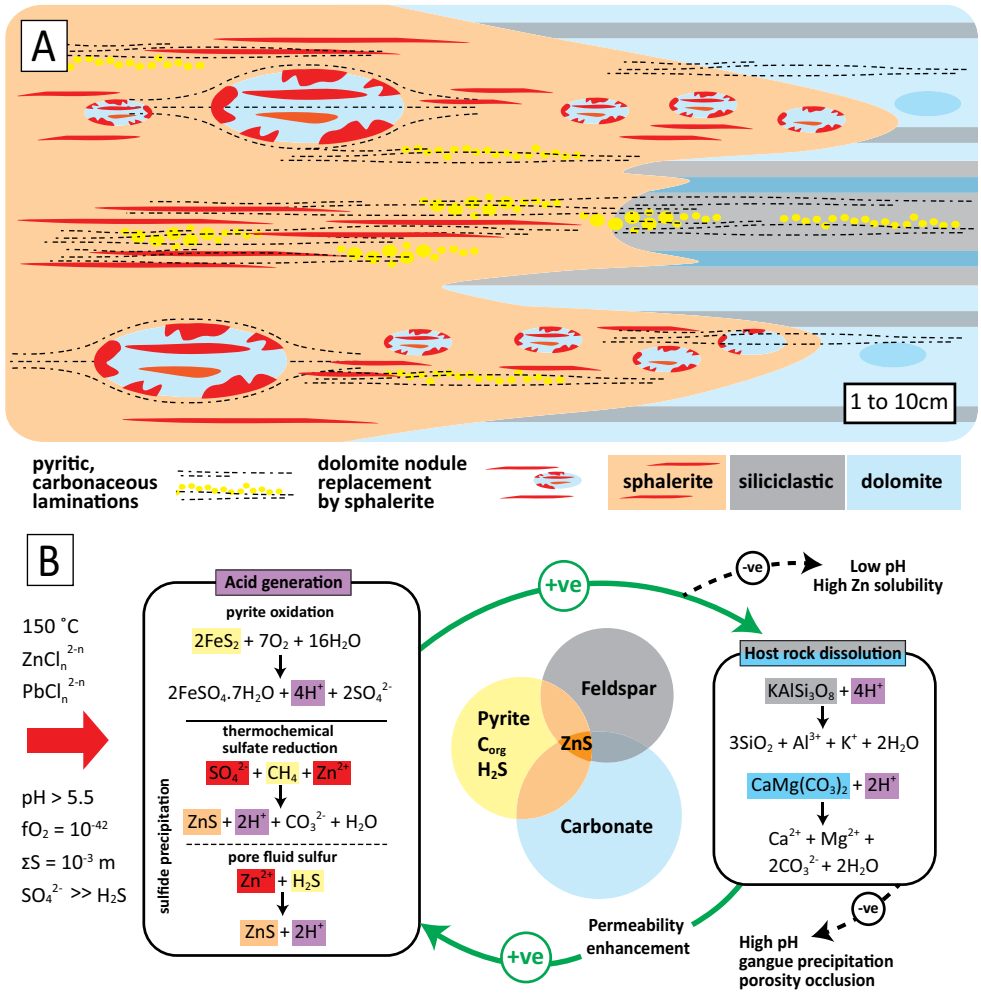

Fig. 10. (A) A cartoon depicting the partial replacement of a mixed siliciclastic-carbonate interval by sphalerite. (B) The self-sustaining chemical reactions that are initiated as an oxidized hydrothermal fluid (red arrow, left-hand side) reacts with different components of the Lower HYC unit. The Venn diagram indicates the Goldilocks zone where the positive feedbacks (green arrows) are optimized and negative feedbacks (black arrows) are minimized. The other colors correspond with the different components of the system. The purple highlights the acid generation in each reaction, the red highlights the components that are introduced by the hydrothermal fluid, and the yellow and orange represent the reduced components in the host rock.

Shale unit that hosts the deposits in the Zambian Cu belt contains abundant feldspar and carbonate, which are considered to have buffered the pH and prevented the development of widespread sericite alteration during ore-stage mineralization (Selley et al., 2005). All of these deposits formed when oxidized ore fluids moved across stratigraphic redox boundaries, which likely initiated a series of self-sustaining reactions that resulted in the transient development of strong horizontal reaction permeability (e.g., Fig. 10).

Conclusions

The stratiform mineralization in the Teena CD-type Zn deposit formed when a series of self-sustaining chemical reactions developed between an oxidized hydrothermal fluid and an organic-rich carbonate-siliciclastic protolith. In the underlying footwall stratigraphic sequence, the input hydrothermal fluid was likely buffered to a weakly acidic pH (>5.5–6) during equilibration with predominantly siliciclastic aquifer units. However, once the hydrothermal fluid crossed a stratigraphic redox boundary in the Teena subbasin, local ore-forming parameters (fo_2-pH) were controlled by a series of self-sustaining reactions involving the main mineralogical and organic components in the protolith. Preenrichment of pyrite during the initial stages of hydrothermal activity increased the mineral reactive surface area in the protolith, thereby enhancing the capacity for local acid generation from pyrite oxidation during subsequent fluid-rock interaction. Sphalerite precipitation resulted in further in situ acid generation, which contributed to host-rock dissolution and the development of transient reaction permeability. Carbonate-poor beds would have provided hot spots for acid generation during infiltration of oxidized hydrothermal fluids, contributing to the local dissolution of K-feldspar and more widespread dissolution of adjacent carbonate-rich beds. The self-sustaining reactions developed in a Goldilocks zone with an optimal abundance and mix of carbonate, feldspar, pyrite, and organic carbon that

permitted long-range intraformational reactive transport and are likely relevant to other sediment-hosted base metal deposits hosted by mixed carbonate-siliciclastic units.

Acknowledgments

The Helmholtz-Rekrutierungsinitive is gratefully acknowledged for funding research for Joe Magnall and Sarah Gleeson. Teck funded the exploration work, with contributions from Rox Resources Limited in the early stages. Teck also supported internal research and provided permission to publish. We are also grateful to Giuseppina Balassone and Erin Marsh for their constructive reviews and Larry Meinert for his editorial handling.

REFERENCES

Alonso-Azcárate, J., Rodas, M., Fernández-Díaz, L., Bottrell, S.H., Mas, J.R., and López-Andrés, S., 2001, Causes of variation in crystal morphology in metamorphogenic pyrite deposits of the Cameros basin (N Spain): Geological Journal , v. 36, p. 159–170.

Altree-Williams, A., Pring, A., Ngothai, Y., and Brugger, J., 2015, Textural and compositional complexities resulting from coupled dissolution-reprecipitation reactions in geomaterials: Earth-Science Reviews, v. 150, p. 628–651.

Barrie, C.D., Boyce, A.J., Boyle, A.P., Williams, P.J., Blake, K., Ogawara, T., Akai, J., and Prior, D.J., 2009, Growth controls in colloform pyrite: American Mineralogist, v. 94, p. 415–429.

Beckingham, L.E., Mitnick, E.H., Steefel, C.I., Zhang, S., Voltolini, M., Swift, A.M., Yang, L., Cole, D.R., Sheets, J.M., Ajo-franklin, J.B., and Depaolo, D.J., 2016, Evaluation of mineral reactive surface area estimates for prediction of reactivity of a multi-mineral sediment: Geochimica et Cosmochimica Acta, v. 188, p. 310–329.

Bethke, C.M., 2007, Geochemical and biogeochemical reaction modeling, 2nd ed.: Cambridge, Cambridge University Press, 542 p.

Borg, G., Piestrzynski, A., Bachmann, G.H., Puttmann, W., Walther, S., and Fiedler, M., 2012, An overview of the European Kupferschiefer deposits: Society of Economic Geologists, Special Publication 16, p. 455–486.

Butler, I.B., and Rickard, D., 2000, Framboidal pyrite formation via the oxidation of iron (II) monosulfide by hydrogen sulphide: Geochimica et Cosmochimica Acta, v. 64, p. 2665–2672.

Chen, J., Walter, M.R., Logan, G.A., Hinman, M.C., and Summons, R.E., 2003, The Paleoproterozoic McArthur River (HYC) Pb/Zn/Ag deposit of northern Australia: Organic geochemistry and ore genesis: Earth and Planetary Science Letters, v. 210, p. 467–479.

Chouinard, A., Paquette, J., and Williams-Jones, A.E., 2005, Crystallographic controls on trace-element incorporation in Auriferous pyrite from the Pascua epithermal high-sulfidation deposit, Chile-Argentina: The Canadian Mineralogist, v. 43, p. 951–963.

Cooke, D.R., Bull, S.W., Large, R.R., and McGoldrick, P.J., 2000, The importance of oxidized brines for the formation of Australian Proterozoic stratiform sediment-hosted Pb-Zn (sedex) deposits: Economic Geology, v. 95, p. 1–18.

Corbella, M., Ayora, C., and Cardellach, E., 2004, Hydrothermal mixing, carbonate dissolution and sulfide precipitation in Mississippi Valley-type deposits: Mineralium Deposita, v. 39, p. 344–357.

Davidson, G.J., 1998, Alkali alteration styles and mechanisms, and their implications for a "brine factory" source of base metals in the rift-related McArthur group, Australia: Australian Journal of Earth Sciences, v. 45, p. 33–49.

Frau, F., 2000, The formation-dissolution-precipitation cycle of melanterite at the abandoned pyrite mine of Genna Luas in Sardinia, Italy: Environmental implications: Mineralogical Magazine, v. 64, p. 995–1006.

Hanor, J.S., 2001, Reactive transport involving rock-buffered fluids of varying salinity: Geochimica et Cosmochimica Acta, v. 65, p. 3721–3732.

Hayward, N., Magnall, J.M., Taylor, M., King, R., McMillan, N., and Gleeson, S.A., 2021, The Teena Zn-Pb deposit (McArthur basin, Australia). Part I: Syndiagenetic base metal sulfide mineralization related to dynamic subbasin evolution: Economic Geology, v. 116, p. 1743–1768.

Idnurm, M., 2000, Towards a high resolution Late Palaeoproterozoic-earliest Mesoproterozoic apparent polar wander path for northern Australia: Australian Journal of Earth Sciences, v. 47, p. 405–429.

Ireland, T., Large, R.R., McGoldrick, P., and Blake, M., 2004, Spatial distribution patterns of sulfur isotopes, nodular carbonate, and ore textures in the McArthur River (HYC) Zn-Pb-Ag deposit, Northern Territory, Australia: Economic Geology, v. 99, p. 1687–1709.

Jerz, J.K., and Rimstidt, J.D., 2003, Efflorescent iron sulfate minerals: Paragenesis, relative stability, and environmental impact: American Mineralogist, v. 88, p. 1919–1932.

Joeckel, R.M., Ang Clement, B.J., and VanFleet Bates, L.R., 2005, Sulfate-mineral crusts from pyrite weathering and acid rock drainage in the Dakota Formation and Graneros shale, Jefferson County, Nebraska: Chemical Geology, v. 215, p. 433–452.

Kunzmann, M., Schmid, S., Blaikie, T.N., and Halverson, G.P., 2019, Facies analysis, sequence stratigraphy, and carbon isotope chemostratigraphy of a classic Zn-Pb host succession: The Proterozoic middle McArthur Group, McArthur basin, Australia: Ore Geology Reviews, v. 106, p. 150–175.

Kunzmann, M., Crombez, V., Blaikie, T.N., Catuneanu, O., King, R., Halverson, G.P., Schmid, S., and Spinks, S.C., 2022, Sequence stratigraphy of the ca. 1640 Ma Barney Creek Formation, McArthur basin, Australia: Australian Journal of Earth Sciences, p. 1–29, doi: 10.1080/08120099.2022.2095030.

Large, R.R., Bull, S.W., Cooke, D.R., and McGoldrick, P.J., 1998, A genetic model for the HYC deposit, Australia: Based on regional sedimentology, geochemistry, and sulfide-sediment relationships: Economic Geology, v. 93, p. 1345–1368.

Large, R.R., Bull, S.W., and Winefield, P.R., 2001, Carbon and oxygen isotope halo in carbonates related to the McArthur river (HYC) Zn-Pb-Ag deposit, North Australia: Implications for sedimentation, ore genesis, and mineral exploration: Economic Geology, v. 96, p. 1567–1593.

Leach, D.L., Bradley, D.C., Huston, D., Pisarevsky, S.A., Taylor, R.D., and Gardoll, S.J., 2010, Sediment-hosted lead-zinc deposits in Earth history: Economic Geology, v. 105, p. 593–625.

Lee, M.R., and Parsons, I., 2003, Microtextures of authigenic Or-rich feldspar in the Upper Jurassic Humber Group, UK North Sea: Sedimentology, v. 50, p. 597–608.

Liu, W., Spinks, S.C., Glenn, M., Macrae, C., and Pearce, M.A., 2021, How carbonate dissolution facilitates sediment-hosted Zn-Pb mineralization: Geology, v. 49, p. 1363–1368.

Loucks, R.G., Reed, R.M., Ruppel, S.C., and Hammes, U., 2012, Spectrum of pore types and networks in mudrocks and a descriptive classification for matrix-related mudrock pores: American Associaton of Petroeum Geologists Bulletin, v. 96, p. 1071–1098.

Magnall, J.M., Gleeson, S.A., Hayward, N., and Rocholl, A., 2020, Massive sulfide Zn deposits in the Proterozoic did not require euxinia: Geochemical Perspectives Letters, v. 13, p. 19–24.

Magnall, J.M., Hayward, N., Gleeson, S.A., Schleicher, A., Dalrymple, I., King, R., and Mahlstadt, N., 2021, The Teena Zn-Pb deposit (McArthur basin, Australia). Part II: carbonate replacement sulfide mineralization during burial diagenesis—implications for mineral exploration: Economic Geology, v. 116, p. 1769–1801.

Magnall, J.M., Gleeson, S.A., Hayward, N., and Oelze, M., 2022, Using whole rock and in situ pyrite chemistry to evaluate authigenic and hydrothermal controls on trace element variability in a Zn mineralized Proterozoic subbasin: Geochimica et Cosmochimica Acta, v. 318, p. 366–387.

Murowchick, J., and Barnes, H.L., 1987, Effects of temperature and supersaturation on pyrite morphology: American Mineralogist, v. 72, p. 1241–1250.

Ortoleva, P., Merino, E., Moore, C., and Chadam, J., 1987, Geochemical self-organization I; reaction-transport feedbacks and modeling approach: American Journal of Science, v. 287, p. 979–1007.

Oszczepalski, S., 1999, Origin of the Kupferschiefer polymetallic mineralization in Poland: Mineralium Deposita, v. 34, p. 599–613.

Page, R.W., and Sweet, I.P., 1998, Geochronology of basin phases in the western Mt. Isa inlier, and correlation with the McArthur basin: Australian Journal of Earth Sciences, v. 45, p. 219–232.

Page, R.W., Jackson, M.J., and Krassay, A.A., 2000, Constraining sequence stratigraphy in north Australian basins: SHRIMP U-Pb zircon geochronology between Mt. Isa and McArthur river: Australian Journal of Earth Sciences, v. 47, p. 431–459.

Pietsch, B.A., Rawlings, D.J., Creaser, P.M., Kruse, P.D., Ahmad, M., Ferenczi, P.A., and Findhammer, T.L.R., 1991, Bauhinia Downs SE53-3: 1:250,000 Geological Map Series, Explanatory Notes: Government Printer of the Northern Territory, 76 p.

Plumb, K.A., Derrick, G.M., and Wilson, I.H., 1980, Precambrian geology of the McArthur River-Mount Isa region, northern Australia, *in* Henderson,

R.A., and Stephenson, P.J., eds., The geology and geophysics of northeastern Australia: Brisbane, Geological Society of Australia, Queensland Division, v. 4, p. 71–88.
Polito, P.A., Kyser, T.K., and Jackson, M.J., 2006, The role of sandstone diagenesis and aquifer evolution in the formation of uranium and zinc-lead deposits, southern McArthur basin, Northern Territory, Australia: Economic Geology, v. 101, p. 1189–1209.
Putnis, A., 2009, Mineral replacement reactions: Reviews in Mineralogy and Geochemistry, v. 70, p. 87–124.
Rieger, P., Magnall, J.M., Gleeson, S.A., Schleicher, A.M., Bonitz, M., and Lilly, R., 2021, The mineralogical and lithogeochemical footprint of the George Fisher Zn-Pb-Ag massive sulphide deposit in the Proterozoic Urquhart Shale Formation, Queensland, Australia: Chemical Geology, v. 560, article 119975.
Rox Resources, 2016, JORC mineral resource estimate completed by independent international consultants, AMEC Foster Wheeler: ASX Press Release, June 1, 2016, 21 p.
Rye, D.M., and Williams, N., 1981, Studies of the base metal sulfide deposits at McArthur River, Northern Territory, Australia: III. The stable isotope geochemistry of the H.Y.C., Ridge, and Cooley deposits: Economic Geology, v. 76, p. 1–26.
Seewald, J.S., Reeves, E.P., Bach, W., Saccocia, P.J., Craddock, P.R., Walsh, E., Shanks, W.C., Sylva, S.P., Pichler, T., and Rosner, M., 2019, Geochemistry of hot-springs at the SuSu Knolls hydrothermal field, Eastern Manus basin: Advanced argillic alteration and vent fluid acidity: Geochimica et Cosmochimica Acta, v. 255, p. 25–48.
Selley, D., Broughton, D., Scott, R., Hitzman, M., Bull, S., Large, R., McGoldrick, P., Croaker, M., Pollington, N., and Barra, F., 2005, A new look at the geology of the Zambian Copperbelt: Economic Geology 100th Anniversary Volume, p. 965–1000.
Southgate, P.N., Bradshaw, B.E., Domagala, J., Jackson, M., Idnurm, M., Krassay, A.A., Page, R.W., Sami, T.T., Scott, D.L., Lindsay, J.F., McConachie, B.M., and Tarlowski, C.Z., 2000, Chronostratigraphic framework for Palaeoproterozoic rocks (1730–1575 Ma) in northern Australia and their implications for base-metal mineralisation: Autralian Journal of Earth Sciences, v. 47, p. 461–483.
Spinks, S.C., Schmid, S., Pagés, A., and Bluett, J., 2016, Evidence for SEDEX-style mineralization in the 1.7 Ga Tawallah Group, McArthur basin, Australia: Ore Geology Reviews, v. 76, p. 122–139.
Spinks, S.C., Pearce, M.A., Liu, W., Kunzmann, M., Ryan, C.G., Moorhead, G.F., Kirkham, R., Blaikie, T., Sheldon, H.A., Schaubs, P.M., and Rickard, W.D.A., 2021, Carbonate replacement as the principal ore formation process in the Proterozoic McArthur River (HYC) sediment-hosted Zn-Pb deposit, Australia: Economic Geology, v. 116, p. 693–718.
Steefel, C.I., Beckingham, L.E., and Landrot, G., 2015, Micro-continuum approaches for modeling pore-scale geochemical processes: Reviews in Mineralogy and Geochemistry, v. 80, p. 217–246.
Vinnichenko, G., Hope, J.M., Jarrett, A.J.M., Williams, N., and Brocks, J.J., 2021, Reassessment of thermal preservation of organic matter in the Paleoproterozoic McArthur River (HYC) Zn-Pb ore deposit, Australia: Ore Geology Reviews, v. 133, article 104129.
Waldmann, S., Busch, A., Van Ojik, K., and Gaupp, R., 2014, Importance of mineral surface areas in Rotliegend sandstones for modeling CO_2-water-rock interactions: Chemical Geology, v. 378–379, p. 89–109.
Wilkinson, J.J., 2013, Sediment-hosted zinc-lead mineralization: Processes and perspectives, *in* Turekian, K., and Holland, H., eds., Treatise on geochemistry, 2nd ed.: Elsevier, p. 219–249.
Williams, N., 1978, Studies of the base metal sulfide deposits at McArthur River, Northern Territory, Australia; I, The Cooley and Ridge deposits: Economic Geology, v. 73, p. 1005–1035.
Wirth, R., 2009, Focused ion beam (FIB) combined with SEM and TEM: Advanced analytical tools for studies of chemical composition, microstructure and crystal structure in geomaterials on a nanometre scale: Chemical Geology, v. 261, p. 217–229.
Xing, Y., Brugger, J., Etschmann, B., Tomkins, A.G., Frierdich, A.J., and Fang, X., 2021, Trace element catalyses mineral replacement reactions and facilitates ore formation: Nature Communication, v. 12, p. 1–7.
Yardley, B.W.D., 2005, 100th anniversary special paper: Metal concentrations in crustal fluids and their relationship to ore formation: Economic Geology, v. 100, p. 613–632.
Yuan, G., Cao, Y., Cluyas, J., Li, X., Xi, K., Wang, Y., Jia, Z., Sun, P., and Oxtoby, N.H., 2015, Feldspar dissolution, authigenic clays, and quartz cements in open and closed sandstone geochemical systems during diagenesis: Typical examples from two sags in Bohai Bay basin, East China: American Association of Petroleum Geologists Bulletin, v. 99, p. 2121–2154.
Yuan, G., Cao, Y., Schulz, H.M., Hao, F., Gluyas, J., Liu, K., Yang, T., Wang, Y., Xi, K., and Li, F., 2019, A review of feldspar alteration and its geological significance in sedimentary basins: From shallow aquifers to deep hydrocarbon reservoirs: Earth-Science Reviews, v. 191, p. 114–140.
Zheng, Y.F., and Hoefs, J., 1993, Carbon and oxygen isotopic covariations in hydrothermal calcites: Theoretical modeling on mixing processes and application to Pb-Zn deposits in the Harz Mountains, Germany: Mineralium Deposita, v. 28, p. 79–89.

Joe Magnall is a postdoctoral research scientist at the GFZ Helmholtz Centre in Potsdam (Germany). Before moving to Germany, Joe completed his B.Sc. (environmental geology) and M.Sc. (geochemistry) degrees at the University of Leeds (UK) and his Ph.D. degree at the University of Alberta (Canada). Joe's research is primarily focused toward developing a better understanding of some of the fundamental aspects of sediment-hosted mineral systems, including the temporal and spatial distribution of deposits and the specific parameters that control the formation of high-grade systems. Up to this point, Joe has worked on deposits from world-class Zn districts in the Canadian Cordillera and northern Australia and typically enjoys combining field geology, petrographic techniques, and multiple types of geochemical data.